High-Resolution Imaging Using a Wideband MIMO Radar System With Two Distributed Arrays

Dang-wei Wang, Xiao-yan Ma, A.-Lei Chen, and Yi Su, *Member, IEEE*

***Abstract*—Imaging a fast maneuvering target has been an active research area in past decades. Usually, an array antenna with multiple elements is implemented to avoid the motion compensations involved in the Inverse synthetic aperture radar (ISAR) imaging. Nevertheless, there is a price dilemma due to the high level of hardware complexity compared to complex algorithm implemented in the ISAR imaging system with only one antenna. In this paper, a wideband multiple-input multiple-output (MIMO) radar system with two distributed arrays is proposed to reduce the hardware complexity of the system. Furthermore, the system model, the equivalent array production method and the imaging procedure are presented. As compared with the classical real aperture radar (RAR) imaging system, there is a very important contribution in our method that the lower hardware complexity can be involved in the imaging system since many additive virtual array elements can be obtained. Numerical simulations are provided for testing our system and imaging method.**

***Index Terms*—Inverse synthetic aperture radar (ISAR), multiple-input and multiple-output (MIMO) radar, radar imaging, real aperture radar (RAR).**

I. Introduction

HIGH-resolution radar images show the distribution property of high energy scatterers of an interest target and therefore, can be widely applied in remote sensing, diagnostic analyzing, and target identifying [1]–[13]. Usually, a 2-D radar image is mapped onto a range and cross-range plane. The range resolution of a radar image is directly related to the bandwidth of the transmitting signal, and the cross-range resolution is determined by the effective length of the antenna aperture. Therefore, to achieve the high cross-range resolution, a synthetic aperture (SA) antenna array without the large physical aperture [1]–[6] or real aperture (RA) antenna array with the large physical aperture [7]–[13] has to be utilized.

In general, one antenna is usually implemented in a SA imaging system, and the efficient array can be produced by the relative rotation between the radar and the target. Ideally, if the target has a uniform Doppler frequency over a small angular aperture and the scatterers can remain in their range cells during the imaging time, a high-quality focused image of target can be easily obtained through the simple Range-Doppler algorithm [2], [3]. However, unfortunately, actual targets observed by a radar system rarely have such an ideal motion. Targets are often engaged in complicated maneuvers that combine translational and rotational motions. The scatterers can drift out of their range cells and their Doppler frequency shifts are time-varying. Consequently, a two-step algorithm including both translational and rotational motion compensations has to be usually considered against the complicated maneuvers [14]–[20]. Nevertheless, although these motion compensation methods can be efficient for some imaging applications, there still exist several important issues that have to be faced by the methods. For example, the parameter estimation accuracy associated with the translational motion compensation [15]–[17] can be affected by the noise in the received signature, and estimation errors could result into an additive image blurring in a low signal-noise-ratio (SNR) environment. On the other hand, for the rotational motion compensation, the nonparametric method, such as the Wigner-Ville distribution (WVD) method in [18], cannot preserve the phase information of the original image and the achievable cross-range resolution is less than the full angular aperture of the original data. Furthermore, the parametric methods based on the adaptive time-frequency distributions [19], [20] are strongly dependent on the assumed motion model and the target geometry. They could become inaccurate when the motion model is not be satisfied. Therefore, an imaging method without the motion compensations can be more desirable.

Different from the SA imaging, an array antenna with multiple elements is often implemented in a RA imaging system [7]–[13]. The target information can be sampled in a parallel manner by a real aperture antenna array during a single snapshot illumination, instead of the spatial sequential sampling with an equivalence array during multiple snapshot illuminations in SA system. Since the array parameters of a real aperture antenna are known, the phase information associated with the measurement channels is determinism during a single snapshot illumination and the target motion can be ignored due to such a fact that the electromagnetic wave speed is far higher than one of the target motion. Therefore, the motion compensations involved in the SA imaging system can be avoided. Nevertheless, it is worth noting that there is a price dilemma due to the high level of hardware complexity compared to complex algorithm implemented in the SA imaging system with only one antenna. Thus, an important issue about the array parameters has to be considered when a real aperture radar system is to image an aerial

Manuscript received November 25, 2008; revised July 30, 2009. First published December 31, 2009; current version published April 16, 2010. This work was supported in part by the National Natural Science Foundation of China under Grant 60772152. The associate editor coordinating the review of this manuscript and approving it for publication was Dr. John Kerekes.

D.-w. Wang and X.-y. Ma were with the Department of information and Command Automation, Wuhan Radar Academy, Wuhan, 430019, China (e-mail: wdwjane@tom.com).

A.-L. Chen was with the Department of Graduate Management, Wuhan Radar Academy, Wuhan, 430019, China (e-mail: chenalei2006@163.com).

Y. Su was with the School of Electronic Science and Engineering, National University of Defense Technology, Changsha 410073, China (e-mail: y.su@yeah.net).

Digital Object Identifier 10.1109/TIP.2009.2039623

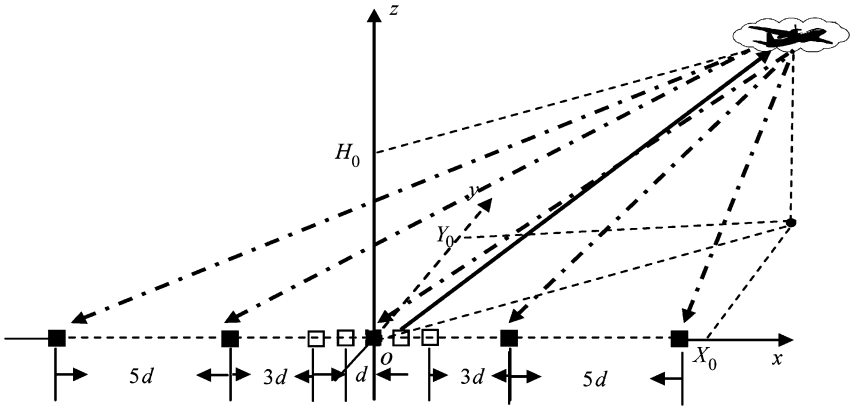

Fig. 1. Array configuration example with five transmitting elements and five receiving elements: ■ receiving element; □ transmitting element; ■ multiplexing element.

target, where microwave array antenna must be hundreds of elements and meters in size in order to obtain a fine cross-range resolution.

Considering the difficulties, as one of the contributions of this paper, we propose a high-resolution imaging method using a wideband MIMO radar system with two distributed real aperture arrays to reduce the hardware complexity of the traditional RA imaging system. Different from the traditional single-channel radar system, such as the ISAR and phase-controlled radar, a classical MIMO radar system transmits and receives simultaneously multiple orthogonal spectrum-shared waveforms from multiple phase centers and to process them [21]–[26]. Due to the orthogonal nature of the transmitting waveforms, many additive virtual array elements can usually be obtained in the system [23]. Furthermore, as demonstrated in this paper, when two distributed antenna array along a same straight line are used, a multiplexing uniform liner array with many additive virtual array elements can be equivalently produced by two distributed array through a proper adjustment procedure. The blank locations in the real array can be filled in by additive virtual array elements. Therefore, an array with fewer elements can be adopted in the proposed method for a desired cross-range resolution and the hardware complexity of the imaging system can be significant reduced, compared with the RA imaging system in [7]–[9] and [13]. In addition, similar to the method proposed in [8] and [13], the complex motion compensations in classical ISAR imaging can be also avoided due to the real aperture nature of the proposed method. Consequently, one might witness a more promising imaging method for targets with complicated maneuvers.

The remainder of the text is organized as follows. In Section II, we give the system model and construct the signal model for our imaging problem. In Section III, we present an adjustment procedure to produce an equivalent uniform array. In Section IV, we develop the range alignment and cross-range imaging formulations for our imaging application. Furthermore, we examine some practical issues on the proposed method, such as the cross-range resolution and the required size of antenna array, as well as its sampling interval and element numbers in Section V. In Section VI, Several numerical examples are presented for testing our method. Finally, conclusions are summarized in Section VII.

II. System Model

Let us considering the 3-D spatial domain (x, y, z) where the variables x, y and z, respectively, identify the horizontal, vertical cross-range and height. Two uniform linear arrays with the different element interval and the same element number are located on the x axis and centered at the origin, which are respectively as the transmitting array and the receiving array. As an example, an array configuration with five transmitting elements and five receiving elements is shown in Fig. 1. For the transmitting array, array length is $2L_T$, element interval is d and element number is N_T. The array's element is identified by the spatial coordinate $(x_p, 0, 0)$, $x_p \in [-L_T, L_T]$. The radiation pattern of the array element is omnidirectional and the transmitted energy is evenly distributed in space. The transmitting waveform $s_p(t)$ of pth element in the transmitting array is a wideband orthogonal ploy phase coded waveform sharing the same spectrum $[f_c - f_0, f_c + f_0]$. Its orthogonal ploy phase sequence set with length of M is denoted as $\{\varphi_p^m, m = 1, 2, \cdots, M\}$. For the receiving array, array length is $2L_R$, element interval is $N_T d$ and element number is equal to the element number of the transmitting array, e.g., $N_R = N_T$ since a uniform sampling procedure of the phase information are required when a regular Fourier transformation is used for cross-range imaging. The array's element is identified by the spatial coordinate $(x_q, 0, 0)$, $x_q \in [-L_R, L_R]$. Furthermore, at each of the element, the received signals are compressed by the filter bank, where every filter in the filter bank is matched to one of the transmitting waveforms. The block diagram of this receiver processing is shown in Fig. 2, where the signal processing of a receiver consists of the baseband converter followed by a matched filter bank.

As is well known, the target can be modeled as multiple scatterers when the wavelength of the carrier frequency is enough small and far less than the electric size of the target. Let us assume that there exist a group of scatterers which are located at the coordinate (x_n, y_n, z_n) and fall within the following cross-range intervals:

$$x_n \in [X_0 - L_{x0}, X_0 + L_{x0}] \tag{1}$$

$$y_n \in [Y_0 - L_{y0}, Y_0 + L_{y0}] \tag{2}$$

$$\text{and } z_n \in [Z_0 - L_{h0}, Z_0 + L_{h0}], \quad n = 1, 2, \cdots \tag{3}$$

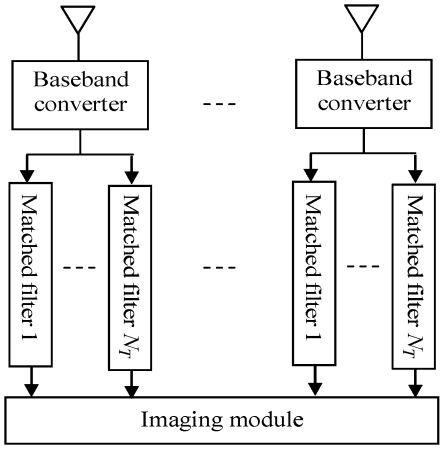

Fig. 2. Block diagram of the receiver processing.

where L_{x0}, L_{y0}, and L_{h0} are called as the half-size of target area in the x, y, and z directions, respectively; X_0, Y_0, and Z_0 are called as the center parameters of the mass of the target area in the x, y, and z directions, respectively.

Considering such a fact that the electromagnetic wave velocity is far higher than radial velocities of the scatterers during a single snapshot illumination, the time delay associated with the target motion can be ignored. Furthermore, in order to simplify our investigations, we also assume that the initial phases of the transmitting waveforms are consistent with each other and the distorted phase associated with the array's element may be negligible. Consequently, when the loss associated with the free-space propagation is not considered, the received echo at the qth element can be expressed via the following formulation:

$$d_q(t,x_q)=\iiint_V \sum_n \sum_p \sigma_{pq}^{(n)}(x,y,z)s_p\left(t-\tau_{pq}^{(n)}\right)dxdydz \tag{4}$$

where V denotes the spatial volume of the target, $\sigma_{pq}^{(n)}(x,y,z)$ denotes the reflectivity associated with the measurement channel from the pth transmitting element to the nth scatterer and then to the qth receiving element, and

$$s_p(t)=\sum_{m=1}^{M}\operatorname{rect}\left[\frac{t-(m-1)T}{T}\right]\exp\left(j2\pi f_c t+j\varphi_p^m\right) \tag{5}$$

$$\tau_{pq}^{(n)}=\frac{R_p^{(n)}+R_q^{(n)}}{c} \tag{6}$$

where f_c denotes the carrier frequency, c denotes the wave propagation speed, T denotes the subpluse width, $R_p^{(n)}$ and $R_q^{(n)}$ denote respectively the distances from the element $(x_p,0,0)$ and the element $(x_q,0,0)$ to the nth scatterer, which are expressed respectively as

$$R_p^{(n)}=\sqrt{(x_p-x_n)^2+(y_n)^2+(z_n)^2} \tag{7}$$

$$R_q^{(n)}=\sqrt{(x_q-x_n)^2+(y_n)^2+(z_n)^2}. \tag{8}$$

Since the array sizes of two distributed antennas are usually far less than the distance from target to the array center for our imaging problem, the effective observation angle is very small. Therefore, the scatterers on the target can be modeled as ideal points without the spatial properties for an enough high carrier frequency, which has been widely used in an imaging radar system [27], [28]. Consequently, the received echo can be simplified as

$$d_q(t,x_q)\approx\sum_n \sigma^{(n)}\sum_p s_p\left(t-\tau_{pq}^{(n)}\right). \tag{9}$$

Moreover, due to the orthogonal property of the transmitting waveforms the baseband signal outputted by the pth filter of the filter bank at the receiving element $(x_q,0,0)$ can be given by

$$d_{pq}(t,x_p,x_q)=\sum_n \sigma^{(n)}r_p\left(t-\tau_{pq}^{(n)}\right)\exp\left(-j\omega_c\tau_{pq}^{(n)}\right) \tag{10}$$

where $r_p(t)$ denotes the autocorrelation function of the waveform transmitted by the element at the spatial coordinate $(x_p,0,0)$, and ω_c is equal to $2\pi f_c$.

Clearly, according to (10), $N_T\times N_R$ independent channels are produced at the receiver due to the orthogonal property of the transmitting waveforms. That is to say, the two-arrays configuration adopted in this paper can extend the array apertures with virtual spatial tapering. Furthermore, as described in the following section, an equivalent multiplexing uniform liner array with the size of $2L_R+2L_T$ and the element interval of d can be obtained when a proper adjustment procedure is utilized.

III. Equivalent Array Production

Recalling the expressions (6)–(8), one can see that the time delays associated with the independent channel are related to both transmitting and receiving element coordinates. Due the different element intervals involved in the transmitting and receiving arrays, the discontinuous time steps can be produced in the time delay $\tau_{pq}^{(n)}$ with the variation of the receiving element coordinate. This will result in the difficulty in cross-range imaging. Therefore, a proper adjustment procedure for a uniform array is necessary for our imaging application. In the following text, we will focus our attention on the adjustment procedure for an equivalent uniform array.

Rewriting the expressions (7) and (8), we can obtain

$$R_p^{(n)}=\sqrt{(x_p)^2-2x_nx_p+(R_n)^2} \tag{11}$$

$$R_q^{(n)}=\sqrt{(x_q)^2-2x_nx_q+(R_n)^2} \tag{12}$$

where the distance R_n denotes the distance from the nth scatterer to the array center and is equal to $\sqrt{(x_n)^2+(y_n)^2+(z_n)^2}$.

Considering the parameters x_p and x_q are usually far less than the distance R_n for a far-field target, one might carry respectively out a series expansion to (11) and (12) in regards of the parameters x_p and x_q at near zero value. If only first three terms of the expression are considered, we can obtain

$$R_p^{(n)}\approx R_n-\frac{x_n}{R_n}x_p+\frac{1}{2}\left(\frac{1}{R_n}-\frac{x_n^2}{R_n^3}\right)x_p^2 \tag{13}$$

$$R_q^{(n)}\approx R_n-\frac{x_n}{R_n}x_q+\frac{1}{2}\left(\frac{1}{R_n}-\frac{x_n^2}{R_n^3}\right)x_q^2. \tag{14}$$

Let us replace the location parameters x_n, y_n and z_n of the scatterer with $x_n=X_0+\overline{x}_n$, $y_n=Y_0+\overline{y}_n$ and $z_n=Z_0+\overline{z}_n$, where $\overline{x}_n\in[-L_{x0},L_{x0}]$, $\overline{y}_n\in[-L_{y0},L_{y0}]$, and $\overline{z}_n\in$

$[-L_{h0}, L_{h0}]$. Consequently, the expression (6) can be rewritten into

$$\tau_{pq}^{(n)} = \frac{1}{c}\left[2R_n - \frac{X_0+\overline{x}_n}{R_n}(x_p+x_q) + \frac{1}{2}\left(\frac{1}{R_n} - \frac{(X_0+\overline{x}_n)^2}{R_n^3}\right)\left(x_p^2+x_q^2\right)\right]. \quad (15)$$

Therefore, one might define the time adjustment function as

$$\tau_{pq} = \frac{1}{c}\left[\frac{X_0}{R_0}(x_p+x_q) + \frac{1}{2}\left(\frac{1}{R_0} - \frac{X_0^2}{R_0^3}\right)\left(x_p^2+x_q^2\right) - \left(\frac{1}{R_0} - \frac{X_0^2}{R_0^3}\right)(x_p+x_q)^2\right] \quad (16)$$

where R_0 denotes the distance from the array center to the center of the mass of the target area and is equal to $\sqrt{(X_0)^2+(Y_0)^2+(Z_0)^2}$.

Furthermore, considering that $X_0 \le R_0$ and the half-sizes of target area are usually far less than the distance from the array center to the mass center of the target area for a far-field target, eg. $\overline{x}_n, \overline{y}_n, \overline{z}_n \ll R_0$. One might obtain the following relationships:

$$R_n \approx R_0 \quad (17)$$

$$\frac{X_0^2}{R_n^3} \approx \frac{\left(X_0+\frac{\overline{x}_n}{2}\right)^2}{R_n^3} \quad (18)$$

and then, we can obtain an adjusted echo with regards to the time variable

$$d'_{pq}(t,x_p,x_q) \approx \sum_n \sigma^{(n)} r_p\left(t-\tau_{pq}^{\prime(n)}\right)\exp\left(-j\omega_c\tau_{pq}^{\prime(n)}\right) \quad (19)$$

where

$$\tau_{pq}^{\prime(n)} \approx \frac{2}{c}\left[R_n - \frac{X_0+\frac{\overline{x}_n}{2}}{R_n}(x_p+x_q) + \frac{1}{2}\left(\frac{1}{R_n} - \frac{\left(X_0+\frac{\overline{x}_n}{2}\right)^2}{R_n^3}\right)(x_p+x_q)^2\right] \quad (20)$$

$$\approx \frac{2}{c}\sqrt{\left[(x_p+x_q) - \left(X_0+\frac{\overline{x}_n}{2}\right)\right]^2 + (y_n)^2 + (z_n)^2}. \quad (21)$$

Obviously, through the time adjustment procedure, we obtain the uniform sample values of the time delay associated with the independent channel. Furthermore, a uniform liner array with the size of $2L_R + 2L_T$ and the element interval of d, where every array element transmits an orthogonal waveform and simultaneously receives its echo through the filter matched to its transmitting waveform, can be equivalently produced by two distributed arrays in our array configuration. Figs. 3 and 4 show an equivalent array example and its receiver structure. As shown in Fig. 3(b), $[N_R \times N_T - (N_R + N_T - 1)]$ additive virtual array elements can be obtained by our MIMO radar and the efficient array size can be extended to $2L_R + 2L_T$ after the time adjustment procedure. This implies that a lower hardware complexity system is involved in our imaging method compared with the methods in [8] and [13]. In additional, Fig. 5 shows the channel distance errors associated with the produced equivalent uniform array and the corresponding real uniform liner array for a single-scatterer target, where the radial distance from the array center to the target is equal to 100 km, and the squint angle away from the z axis direction and level angel from the x axis are $\pi/6$ and 0, respectively. As seen in Fig. 5, the channel distance errors are insignificant when several approximations are used [see for example (13), (14), (21), and so on] and are far less than the radial distance. Therefore, the approximations in the derivation of previously equations can be accepted.

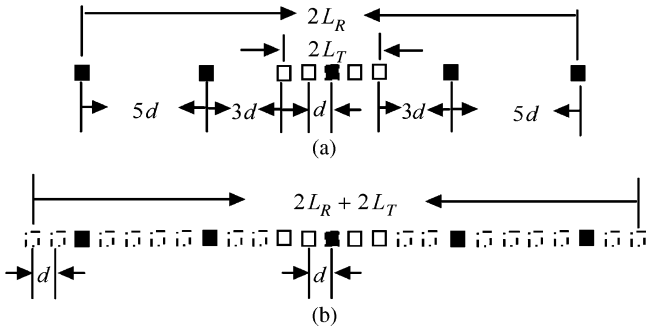

Fig. 3. Equivalent array configuration example with five transmitting elements and five receiving elements. (a) Real array; (b) equivalent array: ■ receiving element; □ transmitting element; ■ multiplexing element; □ virtual array element.

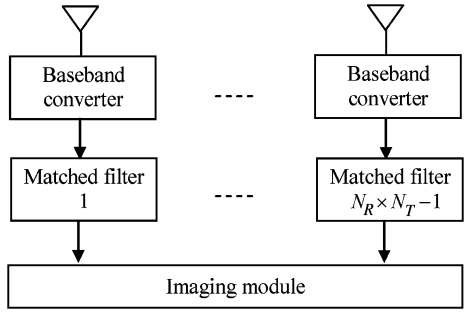

Fig. 4. Receiver structure of equivalent multiplexing array configuration.

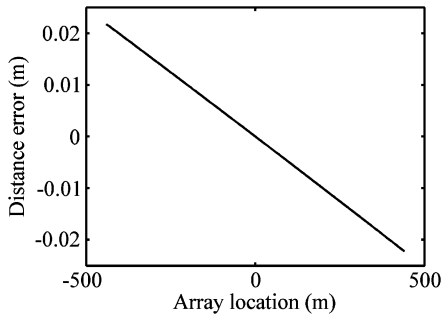

Fig. 5. Distance error associated with the produced equivalent array and the corresponding real array for a single-scatterer target.

IV. Cross-Range Imaging

According to the signal model in (10), one might see that the mainlobe envelopes of the compressed echoes are delayed by the propagation distances associated with the measurement channels. Usually, the range resolution bin of a wideband system is smaller than the distance differences associated with the different measurement channels. For a typical aerial target, the mainlobes of the compressed echoes from the different

filter bands can move through a range resolution bin during the single snapshot. Therefore, in order to obtain fine image, a range alignment procedure of the mainlobe envelope has to be carried out before cross-range imaging.

A. Range Alignment

Rewriting the expression (21), one might obtain

$$\tau_{pq}^{\prime(n)} = \frac{2}{c}\sqrt{(x_p+x_q)^2 - 2\left(X_0 + \frac{\overline{x}_n}{2}\right)(x_p+x_q) + (R_n')^2} \tag{22}$$

where the distance R_n' is equal to

$$\sqrt{(X_0 + (\overline{x}_n/2)^2 + (y_n)^2 + (z_n)^2}.$$

If we replace the equivalent array parameter $x_p + x_q$ with the variable x_q', where $x_q' \in [-(L_T + L_R), (L_T + L_R)]$, and then we can carry out a series expansion to the (22) in regards of the parameter x_q' at near zero value due to the fact that the parameter x_q' is usually far less than the distance R_n' for a far-field target. If only first three terms of the expression are considered, we can obtain

$$\tau_q^{\prime(n)} = \frac{2}{c}\left[R_n' - \frac{X_0 + \frac{\overline{x}_n}{2}}{R_n'}x_q' + \frac{1}{2}\left(\frac{1}{R_n'} - \frac{\left(X_0 + \frac{\overline{x}_n}{2}\right)^2}{R_n'^3}\right)x_q'^2\right]. \tag{23}$$

Since the half-sizes of target area of a far field target are usually far less than the radial distance from the mass center of the target area to the array center, and thus, one might obtain such an approximation as

$$\tau_q^{\prime(n)} \approx \frac{2}{c}\left[-\frac{X_0}{R_0}x_q' + \frac{1}{2}\left(\frac{1}{R_0} - \frac{X_0^2}{R_0^3}\right)x_q'^2\right] + \frac{2}{c}\left(R_n' - \frac{\overline{x}_n}{2R_0}x_q'\right) \tag{24}$$

where R_0 denotes the distance from the array center to the center of the mass of the target area and is equal to $\sqrt{(X_0)^2 + (Y_0)^2 + (Z_0)^2}$.

Usually, the first linear term and first quadratic term in (24) are independent on the variable $\overline{x}_n$ and produce respectively the range migration and curvature associated with the different element along the radial direction. Since the large range migration and curvature may result into a poor cross-range resolution, and thus, they must be corrected in a range-alignment procedure.

If let ω represent the frequency with respect to the time, we define the corrected function as

$$D_1\left(\omega, x_q'\right) = \exp\left[j\frac{2\omega}{c}\left(\frac{X_0}{R_0}x_q' - \frac{1}{2}\left(\frac{1}{R_0} - \frac{X_0^2}{R_0^3}\right)x_q'^2\right)\right] \tag{25}$$

and after multiplying the Fourier transform of the expression (19) with (25), we can obtain a corrected result with regards to the time variable

$$d_q'\left(t, x_q'\right) = \sum_n \sigma^{(n)} r_q\left(t - \frac{2R_n'}{c} + \frac{x_q'\overline{x}_n}{cR_0}\right)\exp\left(-j\omega_c\tau_q^{\prime(n)}\right) \tag{26}$$

where the time delay $2R_n'/c$ is associated with the radial distribution of the nth scatterer and $(x_q'\overline{x}_n)/(cR_0)$ is response to its cross-range distribution associated with the element location of the array. Since x_q' or $\overline{x}_n \ll R_0$ can be always satisfied for a far-field target, the cross-range migration associated with the unknown variable $\overline{x}_n$ is usually less than a range bin. For example, when the equivalent array parameter $L_R + L_T$ and target parameter L_{x0} are equal to 500 m and 30 m respectively, the maximum value of the cross range migration is equal to 0.6 m for a target with the radial distance of 50 km. Therefore, the expression (26) can be further approximated as

$$d_q'\left(t, x_q'\right) \approx \sum_n \sigma^{(n)} r_q\left(t - \frac{2R_n'}{c}\right)\exp\left(-j\omega_c\tau_q^{\prime(n)}\right). \tag{27}$$

This implies that after the previous range alignment is accomplished the mainlobe envelope of the range-compressed echo of a scatterer can remain in the same range bin and the best resolution can be obtained for cross-range imaging.

In additional, one should also see that the previous range alignment is independent on the target motion and the noise in the received echo when the center parameters of the mass of the target area are given beforehand, which is completely different from the translational motion compensation involved in ISAR imaging [14]–[17].

B. Cross-Range Imaging

According to the expression (21), one might see that a general squint case has to be faced for our imaging application when x_n is not equal to zero. Usually, for imaging a squint target, a band conversion of the target area must be carried out beforehand. According to [27], the band conversion of the squint target area in the x_q' domain can be accomplished by

$$d_q^B\left(t, x_q'\right) = d_q'\left(t, x_q'\right)\exp\left(-j2k_c\sin\theta_0 x_q'\right) \tag{28}$$

where $k_c = \omega_c/c$ is the wavenumber related with the carrier frequency, and particularly, for a squint target at the first quadrant

$$\theta_0 = \arctan\left(\frac{X_0}{\sqrt{(Z_0)^2 + (Y_0)^2}}\right). \tag{29}$$

If let k_x represent the spatial frequency with respect to the variable x_q', we can obtain the Fourier transform of the expression (28) via the following Fourier integral:

$$\begin{aligned} D_q(t, k_x) &= \int_{-L_x'}^{L_x'} d_q^B\left(t, x_q'\right)\exp\left(-jk_x x_q'\right)dx_q' \\ &= \sum_n \sigma^{(n)} r_q\left(t - \frac{2R_n'}{c}\right) \\ &\quad \times \int_{-L_x'}^{L_x'} \exp\left[j\phi\left(x_q'\right)\right]dx_q' \end{aligned} \tag{30}$$

where $L_x' = L_R + L_T$ is the half-size of the equivalent array, $\phi(x_q') = -2k_c R_q^{\prime(n)} - 2k_c\sin\theta_0 x_q' - k_x x_q'$ is the phase of the exponential term and $R_q^{\prime(n)} = \sqrt{[x_q' - (X_0 + (\overline{x}_n/2))]^2 + (y_n)^2 + (z_n)^2}$ is the distance from the nth scatterer to the element with the spatial coordinates $(x_q', 0, 0)$.

Since the amplitude of the integrated terms in (30) is constant for the variable x'_q, the major contribution to the integral will come from a small neighborhood near the points where the first derivative of the function $\phi(x'_q)$ vanishes. These points are known as points of stationary phase [11], [27], [28]. Therefore, the asymptotic evaluation of $D_q(t,k_x)$ for a large k_c can be accomplished by finding points of stationary phase in (30) through the first derivative of the phase function. By means of the method stationary phase (MSP) used in [11], [27], and [28], after a slow-fluctuating amplitude factor that does not play an important role in imaging problems has been suppressed for notational simplicity, the evaluation of the integral (30) in can result into the following analytical formula:

$$D_q\left(t,k'_x\right)=\sum_n \sigma^{(n)} r_q\left(t-\frac{2R'_n}{c}\right) \times \exp\left[-jH_1\sqrt{(2k_c)^2-\left(k'_x\right)^2}-jk'_x\left(X_0+\frac{\overline{x}_n}{2}\right)\right] \quad (31)$$

where $H_1=\sqrt{y_n^2+z_n^2}$, $k'_x=(2k_c\sin\theta_0+k_x)\in\Omega_x=\cup_n\Omega_x^{(n)}$ and

$$\Omega_x^{(n)}=\left[2k_c\sin\theta_{\min}^{(n)},2k_c\sin\theta_{\max}^{(n)}\right] \quad (32)$$

is the spatial frequency support domain of the nth scatterer with respect to the array.

Furthermore, we consider such changes of variables as $y_n=Y_0+\overline{y}_n$ ($\overline{y}_n\in[-L_{y0},L_{y0}]$) and $z_n=Z_0+\overline{z}_n$ ($\overline{z}_n\in[-L_{h0},L_{h0}]$), the expression in (31) can be approximated as

$$D_q\left(t,k'_x\right)\approx\sum_n \sigma^{(n)} r_q\left(t-\frac{2R'_n}{c}\right) \times \exp\left[-j\overline{H}_1\sqrt{(2k_c)^2-\left(k'_x\right)^2}-jk'_x\left(X_0+\frac{\overline{x}_n}{2}\right)\right] \quad (33)$$

where $\overline{H}_1=\sqrt{(Y_0)^2+(Z_0)^2}$ and $k'_x\in\overline{\Omega}_x=[2k_c\sin\overline{\theta}_{\min},2k_c\sin\overline{\theta}_{\max}]$. Especially, the smallest and largest aspect angles with respect to the array can be given for a target at the first quadrant by

$$\overline{\theta}_{\min}=\arctan\left(\frac{X_0-L_{x0}-L'_x}{\sqrt{(Y_0)^2+(Z_0)^2}}\right) \quad (34)$$

$$\overline{\theta}_{\max}=\arctan\left(\frac{X_0+L_{x0}+L'_x}{\sqrt{(Y_0)^2+(Z_0)^2}}\right). \quad (35)$$

If the reference signal $D_0(k'_x)$ is defined as

$$D_0\left(k'_x\right)=\exp\left[j\overline{H}_1\sqrt{(2k_c)^2-\left(k'_x\right)^2}+jk'_xX_0\right] \quad (36)$$

and then, one might carry out the pulse compression in the cross-range domain through the reference signal in (36), and obtain

$$D_q^c\left(t,k'_x\right)=\sum_n \sigma^{(n)} r_q\left(t-\frac{2R'_n}{c}\right)\bullet I\left(k'_x\right)\bullet\exp\left(-jk'_x\frac{\overline{x}_n}{2}\right) \quad (37)$$

where

$$I\left(k'_x\right)=\begin{cases}1, & k'_x\in\overline{\Omega}_x=[2k_c\sin\overline{\theta}_{\min},2k_c\sin\overline{\theta}_{\max}]\\ 0, & \text{otherwise.}\end{cases} \quad (38)$$

If let $|\overline{\Omega}_x|$ denote the Doppler bandwidth of $\overline{\Omega}_x$, we can obtain a 2-D image expression via the inverse Fourier transform with regards to the variable k'_x as

$$d_{qq}^c\left(t,x'_q\right)\approx\sum_n \sigma^{(n)} r_q\left(t-\frac{2R'_n}{c}\right)\bullet i_x\left(x'_q-\frac{\overline{x}_n}{2}\right) \quad (39)$$

where

$$i_x\left(x'_q\right)\approx|\overline{\Omega}_x|\exp\left(j\Omega_{xc}x'_q\right)\operatorname{sinc}\left(\frac{|\overline{\Omega}_x|x'_q}{2\pi}\right) \quad (40)$$

and particularly, for a target in the first quadrant

$$\Omega_{xc}=2k_c\sin\theta_0 \quad (41)$$

is the center Doppler frequency associated with the cross-range direction.

Similar to the ISAR imaging and phase-controlled imaging, it can be viewed from the previous equation that the spatial frequency is also limited to the spatial frequency band $[2k_c\sin\overline{\theta}_{\min},2k_c\sin\overline{\theta}_{\max}]$ in our method. This frequency band is twice the band involved in the method [13] when the same array parameters and target location parameters are considered. The cross-range resolution of our method in this paper is as same as the resolution of the ISAR imaging and phase-controlled imaging, but is twice that of the method in [13]. That is to say, in order to obtain a same cross-range resolution, the array size can be reduced to half one of the method in [13]. Particularly, due to the additive virtual array elements, the element number associated with two distributed arrays in our method can reduced to N_R+N_T-1 and is far lower than the number $2\times N$ associated with two perpendicular arrays in [13] (where the element number of one perpendicular arrays is equal to $N=N_R\times N_T$) and N in the phase-controlled imaging method (where the element number of the phase-controlled array is equal to $N=N_R\times N_T$).

In additional, it is worth noting that the image produced by the proposed method is different from one of the methods in [8], [13]. The resulted image of our method is only a reduced version of the real image of the target, where the cross-range location value of a scatterer in the resulted image is half one of the real cross-range location.

V. Resolution and Array Parameter Constraint

A. Resolution

According to the expressions (39) and (40), the cross-range resolution of the resulted image associated with the equivalent array is determined by the mainlobe width of the sinc-like blip. Thus, the cross-range resolution in our method can be given by

$$\Delta_x=\frac{2\pi\rho}{|\overline{\Omega}_x|}=\frac{\pi\rho}{|k_c\sin\overline{\theta}_{\max}-k_c\sin\overline{\theta}_{\min}|} \quad (42)$$

where ρ is the scaled coefficient associated with the mainlobe width of the sinc-like blip and equal to 0.88 when the mainlobe width of 3 dB is measured.

Obviously, the cross-range resolution of the image is related to the size of the array, carrier frequency, target height and squint angle with respect to the array configuration. Furthermore, since

the size of the receiving array is far larger than one of the transmitting array in our method. Therefore, the cross-range resolution of the equivalent array can be mainly improved when the size of the receiving array increases, except that the carrier frequency f_c increases, or the target height Z_0 and the squint angle get smaller.

B. Array Parameter Constraint

Usually, we expect that an image with a cross-range resolution better than a desired value is always held over a given spatial scope. That is to say, the array parameters including the size and element interval of the equivalent antenna array should be constrained. In fact, the minimum size and the maximum element interval of a uniform liner array are respectively constrained by the smallest Doppler bandwidth $\Omega^x_{\min}$ and largest Doppler bandwidth $\Omega^x_{\max}$ over the given spatial scope. Therefore, for a target at the first quadrant, $\Omega^x_{\min}$ and $\Omega^x_{\max}$ involved in the imaging procedure in this paper can be directly expressed as

$$\begin{aligned}\Omega^x_{\min} &= 2k_c \sin\left[\arctan\left(\frac{X_0 + L'_x}{R_{\max}\cos\varphi_{\max}}\right)\right] \\ &\quad - 2k_c \sin\left[\arctan\left(\frac{X_0 - L'_x}{R_{\max}\cos\varphi_{\max}}\right)\right] \qquad (43)\\ \Omega^x_{\max} &= 2k_c \sin\left[\arctan\left(\frac{L'_x}{R_{\min}}\right)\right] \\ &\quad - 2k_c \sin\left[\arctan\left(-\frac{L'_x}{R_{\min}}\right)\right] \qquad (44)\end{aligned}$$

where $R_{\max}$ and $R_{\min}$ denote respectively the furthest and nearest radial distances from the coordinate origin to the center of target area and $\varphi_{\max}$ is the maximum elevation angle away from the z axis.

Therefore, in order to reach a desired cross-range resolution for the alias-free imaging over the given spatial scope, the minimum half-size and maximum element interval of the equivalent linear array should be satisfied with the constrained relationships

$$\Delta_{x0} \le \frac{2\pi\rho}{\Omega^x_{\min}} \qquad (45)$$

$$\Delta L'_x \le \frac{2\pi\rho}{\Omega^x_{\max}} \qquad (46)$$

where Δ_{x0} denotes the worst cross-range resolution desired over the given spatial scope and $\Delta L'_x$ denotes the maximum element interval of the equivalent linear array.

Moreover, it is worth noting that the constrained relationships in (45) and (46) are presented to the equivalent linear array. The additive relationships should be considered for the receiving and transmitting arrays of our imaging system. In fact, according to the array configuration in Fig. 1 and the theoretical expressions in Section III, one might see that the size of the equivalent linear array is the sum of the sizes of the receiving and transmitting arrays, and the element interval is equal to the interval of the transmitting array. Therefore, when the minimum half-size and maximum element interval of the equivalent linear array are calculated through the constrained relationships in (45) and (46), the element numbers of the receiving and transmitting arrays can be given by

$$N_T = N_R = \sqrt{\frac{2L'_{\min}}{\Delta L'_{\max}} + 1} \qquad (47)$$

where $L'_{\min}$ denotes the minimum half-size equivalent linear array.

Then, the half-sizes of the receiving and transmitting arrays can be calculated by

$$L_T = \frac{N_T - 1}{2}\Delta L'_{\max} \qquad (48)$$

$$L_R = \frac{N_R - 1}{2}N_T\Delta L'_{\max}. \qquad (49)$$

That is to say, when the desired cross-range resolution and the spatial scope are given for our imaging method, one might easily calculate the corresponding array parameters of the imaging system.

VI. Simulation Results

In this section, to demonstrate the imaging system and method proposed in this paper, we will contrast the imaging method in this paper with the methods proposed in [8] and [13]. For the sake of notational brevity, the method proposed in this paper will be called as "WMIMO", the method in [13] as "NMIMO" and the phase-controlled method in [8] as "PC" for all later experiments. In additional, simple stochastic ploy phase sequences, which are produced by the expression (50), are used as the code sequences of the transmitting waveforms for the "WMIMO" and "NMIMO"

$$\varphi^m_p = 2\pi\mathrm{randn}(M, 1) \qquad (50)$$

where the function "randn" is a matlab program for the production of Gaussian random variables and M denotes the code length.

A. Comparison of Array Parameters

In this experiment, we consider a simple target only with one ideal scatterer. The radial distance from the array center to the target is equal to 100 km, and the squint angle away from the z axis direction and level angel from the x axis are $\pi/6$ and 0, respectively. For the "WMIMO", wideband shared-spectrum waveforms coded with stochastic ploy phase sequences are employed to illuminate a target. Its carrier frequency is 11.8 GHz and its bandwidth is 150 MHz, which is response to a range resolution ΔR, i.e., 1 m. For the "NMIMO", narrowband shared-spectrum waveforms coded with stochastic ploy phase sequences are employed, the carrier frequency is also 11.8 GHz, and but, the bandwidth is 0.15 MHz, which is response to a poor range resolution ΔR, i.e., 1000 m. Furthermore, for the "PC", the linear frequency modulation waveform with the same carrier frequency and bandwidth as the "WMIMO" is used. Fig. 6 shows the cross-range resolution values with respect to half-size of the equivalent multiplexing array in our method, compared to the resolution values of the "NMIMO" and the "PC". As seen in Fig. 6, the cross-range resolution of the image can be improved with the increasing of the size of the linear arrays

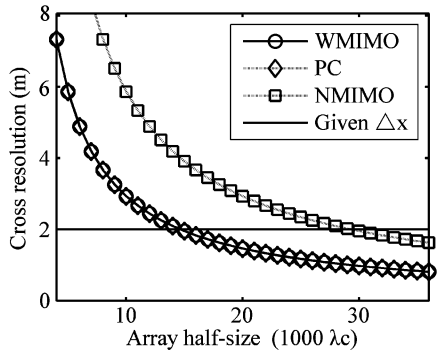

Fig. 6. Cross resolutions with respect to half-length of the array for the carrier frequency of 11.8 GHz.

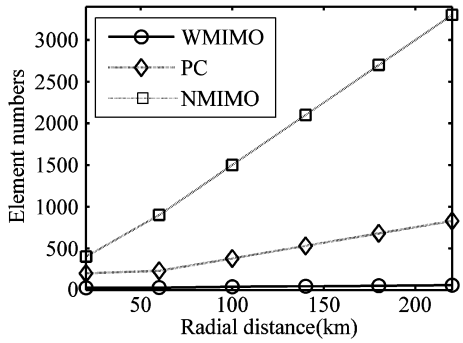

Fig. 7. Element numbers required by three methods for a cross-range resolution of 2 m.

for three methods. For a resolution value of 2 m, the half-size of both equivalent multiplexing array of the "WMIMO" and real aperture array of the "PC" must be longer than 14750 wavelengths which are corresponding to an array with the half-size of 375 m, and but, the half-size of the "NMIMO" must be longer than 29500 wavelengths corresponding to an array with the half-size of 750 m. The equivalent array size of the "WMIMO" and the real aperture array size of the "PC" are only half one of the "NMIMO" for a same resolution. This is due to the fact that the spatial frequency domains associated with both horizontal and vertical cross-range directions in the "NMIMO" are mapped into $k_x = k_c \sin\theta$ and $k_y = k_c \sin\phi$. On the other hand, the spatial frequency domain associated with the cross-range direction in the "WMIMO" and the "PC" is mapped into $k_x = 2k_c \sin\theta$.

Furthermore, Fig. 7 shows the element numbers required by three methods for a resolution value of 2 m when the radial distance values of the target are from 20 to 220 km and other location parameters of the target are unchanged. Obviously, from Fig. 7, although more elements are required by three methods for the given cross-range resolution with the increasing of the radial distance, the element number involved in the "WMIMO" is significantly smaller than that in both the "NMIMO" and the "PC". For example, when radial distance is equal to 100 km and the element interval is 2 m, total element number associated with the receiving and transmitting arrays of the "WMIMO" are only 41, and but, the total numbers of the "NMIMO" and the "PC" are 2×750 and 375, respectively. Obviously, the hard complexity of the imaging system can be significantly reduced in the "WMIMO".

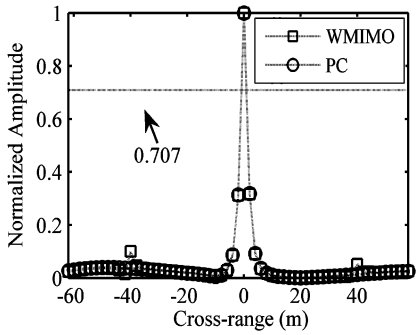

Fig. 8. Cross-range imaging results of two methods.

B. Imaging a Single-Scatterer Target

In this experiment, the simulation parameters are same as the previous experiment, but element numbers associated with both receiving and transmitting arrays of the "WMIMO" are 21, and the half-sizes of two distributed arrays are 420 m and 20 m, respectively, which could result in an equivalent multiplexing array with the half-size of 440 m and element interval of 2 m. Furthermore, for the "PC", the total element number and half-size of every array are 441 and 440 m, respectively. Fig. 8 shows the cross-range imaging results of the "WMIMO" and the "PC". As seen in Fig. 8, the mainlobe width values of imaging results of two methods are identical and are close to the theoretical cross-range resolution. However, different from the "PC", where 441 array elements are involved in its linear array, only 41 array elements are required in the "WMIMO" for the same cross-range resolution, which can be attributed to the fact that 400 additive virtual array elements can be produced in the "WMIMO".

Moreover, Fig. 9(a) and (b) shows the 2-D imaging results for the single-scatterer target when pseudo orthogonal ployphase sequences with the different code lengths are used as the code sequences of the transmitting waveforms for the "WMIMO". As seen in Fig. 9(a) and (b), the target can be correctly identified when simple pseudo orthogonal codes in (50) are used as the code sequences of the proposed "WMIMO". Although pseudo orthogonal property of simple ployphase sequences in (50) results into many sidelobes, one might see such a fact that the sidelobes can be significantly reduced with the increasing of the code length due to the cross-range correlative accumulation at the location of the scatterer. Obviously, these results validate the imaging system and method proposed in this paper.

C. Imaging a Multiple-Scatterers Target

In this experiment, we consider a more complex target scenario and test the resolution ability of the "WMIMO". The geometry model of the target is shown in Fig. 10. The target is composed of eleven ideal scatterers, and the sizes of the target area in the x and y directions are equal to 32 m and 40 m, respectively. The radial distance from the array center to the target is equal to 100 km, and the squint angle away from the z axis direction and level angel from the x axis are $\pi/6$ and $\pi/4$ respectively. The other simulation parameters including the carrier frequency, bandwidth, array size and element interval are as same as the above simulation for the "WMIMO". The imaging results of the "WMIMO" are shown in Fig. 11(a) and (b) when the code length is 256 and 512, respectively. Furthermore, in

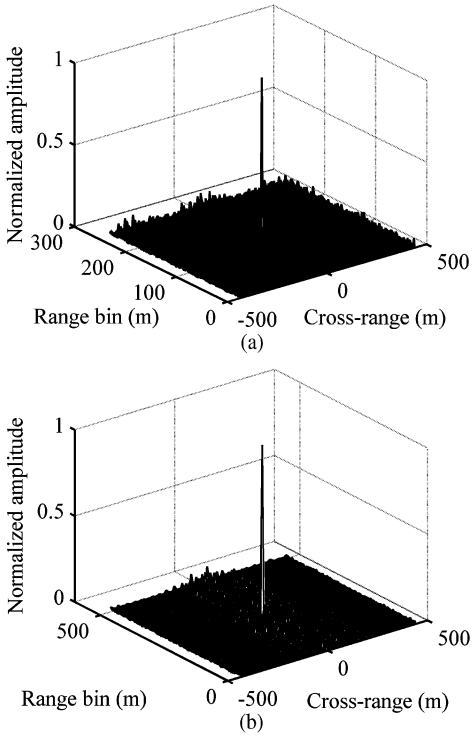

Fig. 9. Mesh graph of imaging results for a single-scatterer target when the code length is equal to (a) 256; (b) 512.

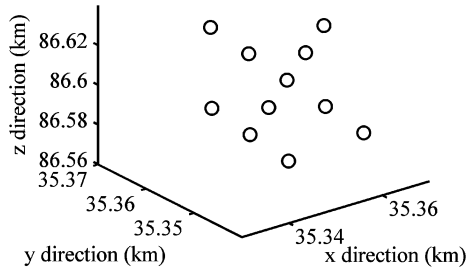

Fig. 10. Target model in the simulations.

order to demonstrate the "WMIMO" proposed in this paper, the original projection image of the target is provided in Fig. 11, where the cross-range center of the original projection image is moved to the array center.

As seen in Fig. 11, the compressed echoes of the target are focused both in the range and cross-range directions for different code lengths. However, although all scatterers on the target body are correctly identified by the method proposed in this paper with an undegradatated resolution, the obtained image is an obviously reduced version of the original projection image of the target. Compared with the original projection image, where the maximum half-size of the target mass is equal to 16 m, the maximum half-size in the image produced by the proposed method is only equal to 8 m. The cross-range location parameter of every scatterer is reduced to half one of the real location. In additional, from Fig. 11(a) and (b), one might see again such a fact that the sidelobes can be significantly reduced with the increasing of the code length. Obviously, the results are consistent with our theoretical formulation in Section IV and the method proposed in this paper is demonstrated further.

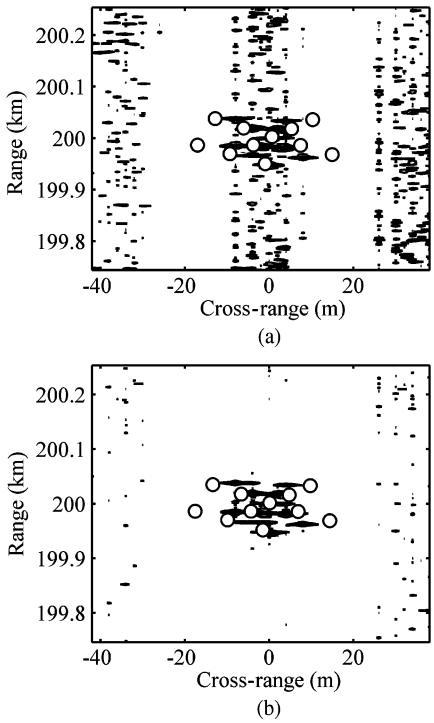

Fig. 11. Imaging results of the "WMIMO" with code length of (a) 256; (b) 512 "O" denotes the original projection location of the scatterer on the imaging plane.

VII. Conclusion

In this paper, a wideband MIMO radar system with two distributed arrays has been investigated to reduce the hardware complexity of the RA imaging system. We set up the signal model for our imaging application, and develop the equivalent array production and cross-range imaging formulations. Furthermore, we also examine the cross-range resolution, the required size and sampling interval of antenna arrays. Similar to the methods in [8] and [13], the complex motion compensations can be also avoided in this method due to the parallel sampling during a single snapshot illumination. However, different from the phase-controlled method in [8] and the method in [13], the system complexity can be significantly reduced in the proposed method due to the additive virtual array elements associated with the proposed method. Simulation results show that the required element number can be reduced by the developed wideband MIMO radar imaging method to about 1/10 of the phase-controlled method in [8] and 1/32 of the method in [13] for a target with the radial distance of 100 km when the cross-range resolution is given.

In additional, it should be pointed out that performance evaluation of the proposed system has only been based on simple targets only with ideal scatterers. The performance verification in Section VI is limited in its meaning. Therefore, future works should be carried out to demonstrate our method with more complicated targets.

Acknowledgment

The authors would like to thank the anonymous reviewers for their constructive comments and suggestions which improved the paper significantly.

REFERENCES

[1] W. M. Brown and R. J. Fredericks, "Range-doppler imaging with motion through resolution cells," *IEEE Trans. Aerosp. Electron. Syst.*, vol. 5, no. 1, pp. 98–102, Jan. 1969.

[2] J. I. Walker, "Range-doppler imaging of rotating objects," *IEEE Trans. Aerosp. Electron. Syst.*, vol. 16, no. 1, pp. 23–52, Jan. 1980.

[3] C. C. Chen and H. C. Andrews, "Target-motion-induced radar imaging," *IEEE Trans. Aerosp. Electron. Syst.*, vol. 16, no. 1, pp. 2–14, Jan. 1980.

[4] J. Nolan and M. Cheney, "Synthetic aperture inversion for arbitrary flight paths and non-flat topography," *IEEE Trans. Image Process.*, vol. 12, no. 9, pp. 1035–1043, Sep. 2003.

[5] K. T. Kim, D. K. Seo, and H. T. Kim, "Efficient classification of ISAR images," *IEEE Trans. Antennas Propagat.*, vol. 53, no. 5, pp. 1611–1621, May 2005.

[6] C. E. Yarman, B. Yazıcı, and M. Cheney, "Bistatic synthetic aperture radar imaging for arbitrary flight trajectories," *IEEE Trans. Image Process.*, vol. 17, no. 1, pp. 84–93, Jan. 2008.

[7] B. Steinberg, "Radar imaging from a distorted array: The radio camera algorithm and experiments," *IEEE Trans. Antennas Propagat.*, vol. 29, no. 5, pp. 740–748, May 1981.

[8] M. Soumekh, "Array imaging with beam-steered data," *IEEE Trans. Image Process.*, vol. 1, no. 3, pp. 379–390, Jul. 1992.

[9] M. Soumekh, "Phased array imaging of moving targets with randomized beam steering and area spotlighting," *IEEE Trans. Image Process.*, vol. 6, no. 5, pp. 736–749, May 1997.

[10] Broquetas, J. Palau, L. Jofre, and A. Cardama, "Spherical wave near field imaging and radar cross-section measurement," *IEEE Trans. Antennas Propagat.*, vol. 46, no. 5, pp. 730–735, May 1998.

[11] J. M. López-Sánchez and J. Fortuny, "3-D radar imaging using range migration techniques," *IEEE Trans. Antennas Propagat.*, vol. 48, no. 5, pp. 728–737, May 2000.

[12] C. Z. Ma, T. S. Yeo, and Q. Zhang *et al.*, "Three-dimensional ISAR imaging based on antenna array," *IEEE Trans. Geosci. Remote Sens.*, vol. 46, no. 2, pp. 504–515, Feb. 2008.

[13] X.-Y. Ma, D.-W. Wang, and Y. Su, "2-D imaging via a narrow-band MIMO radar system," in *Proc. IEEE 9th Int. Conf. Signal Processing*, Beijing, Oct. 2008, pp. 2263–2266.

[14] J. S. Son, G. Thomas, and B. C. Flores, *Range-Doppler Radar Imaging and Motion Compensation*. Boston, MA: Artech House, 2000.

[15] D. E. Wahl, P. H. Eichel, D. C. Ghiglia, and C. V. Jakowatz, Jr., "Phase gradient autofocus—A robust tool for high resolution SAR phase correction," *IEEE Trans. Aerosp. Electron. Syst.*, vol. 30, no. 3, pp. 827–835, Jul. 1994.

[16] F. Berizzi and G. Corsini, "Autofocusing of inverse synthetic aperturradar images using contrast optimization," *IEEE Trans. Aerosp. Electron. Syst.*, vol. 32, no. 3, pp. 1185–1191, Jul. 1996.

[17] X. Li, G. Liu, and J. Ni, "Autofocusing of ISAR images based on entropy minimization," *IEEE Trans. Aerosp. Electron. Syst.*, vol. 35, no. 4, pp. 1240–1252, Oct. 1999.

[18] V. C. Chen and S. Qian, "Joint time-frequency transform for radar range-Doppler imaging," *IEEE Trans. Aerosp. Electron. Syst.*, vol. 34, no. 2, pp. 486–499, Apr. 1998.

[19] Y. X. Wang, H. Ling, and V. C. Chen, "ISAR motion compensation via adaptive joint time-frequency technique," *IEEE Trans. Aerosp. Electron. Syst.*, vol. 34, no. 2, pp. 670–677, Apr. 1998.

[20] L. P. Du and G. C. Su, "Adaptive inverse synthetic aperture radar imaging for nonuniformly moving targets," *IEEE Geosci. Remote Sens. Lett.*, vol. 2, no. 3, pp. 247–249, Jul. 2005.

[21] E. Fishler, A. Haimovich, and R. Blum *et al.*, "MIMO radar: An idea whose time has come," in *Proc. IEEE Radar Conf.*, Apr. 2004, pp. 71–78.

[22] E. Fishler, A. Haimovich, and R. Blum *et al.*, "Spatial diversity in radars—Models and detection performance," *IEEE Trans. Signal Process.*, vol. 54, no. 3, pp. 823–838, Mar. 2006.

[23] I. Bekkerman and J. Tabrikian, "Target detection and localization using MIMO radars and sonars," *IEEE Trans. Signal Process.*, vol. 54, no. 10, pp. 3873–3883, Oct. 2006.

[24] Y. Yang and R. S. Blum, "MIMO radar waveform design based on mutual information and minimum mean-square error estimation," *IEEE Trans. Aerosp. Electron. Syst.*, vol. 43, pp. 330–343, Jan. 2007.

[25] J. Li and P. Stoica, "MIMO radar with colocated antennas," *IEEE Signal Process. Mag.*, vol. 24, no. 5, pp. 106–114, May 2007.

[26] A. Haimovich, R. Blum, and L. Cirnini, "MIMO radar with widely separated antennas," *IEEE Signal Process. Mag.*, vol. 25, no. 1, pp. 116–129, Jan. 2008.

[27] M. Soumekh, *Synthetic Aperture Radar Signal Processing With MATLAB Algorithms*. New York: Wiley, 1999.

[28] Z. Bao, M. D. Xing, and T. Wang, *Radar Imaging Technique*. China: Publish House of Electronics Industry, 2005.

Dang-wei Wang received the B.S. and M.S. degrees from Wuhan Radar Academy, Wuhan, China, in 2000 and 2003, respectively, and the Ph.D. degree from the Department of Electrical and Electronic Engineering, National University of Defense Technology, Changsha, China, in 2006.

He is now a Postdoctorate with the Electronics Institute, Wuhan Radar Academy, Wuhan, China. His research interests include multichannels radar target characteristic, as well as advanced signal processing with application to radar target imaging and identification.

Xiao-yan Ma received the B.S. degree from the ing University of Science and Technology, Nanjing, China, in 1982, the M.S. degree from the National University of Defense Technology, Changsha, China, in 1988, and the Ph.D. degree from Tsinghua University, Beijing, China, in 2002.

He is currently a Professor with the Department of information and command automation, Wuhan Radar Academy, Wuhan, China. His main research interests include radar system, target detection and imaging, as well as ISAR signal processing.

A.-Lei Chen received the B.S. and M.S. degrees from the Wuhan Radar Academy, Wuhan, China, in 2004 and 2007, respectively, where he is currently pursuing the Ph.D. degree.

His research interests include multichannels radar target imaging and identification.

Yi Su (M'03) received the B.S., M.S., and Ph.D. degrees in electrical and electronic engineering from the National University of Defense Technology, Changsha, China, in 1982, 1985, and 2001, respectively.

Since 1986, he has been with the Department of Electrical and Electronic Engineering, National University of Defense Technology. He has served as an Associate Professor since 1993 and is currently a Professor. He joined the Purdue University, West Lafayette, IN, as a research fellow in 1998. His main research interests include radar target characteristics, ground penetrating radar (GPR), and interpretation of SAR imagery.